PANAMGEO CHILE 2024
17th PAN-AMERICAN CONFERENCE ON SOIL MECHANICS AND GEOTECHNICAL ENGINEERING | 2nd LATIN-AMERICAN REGIONAL CONFERENCE OF IAEG
LA SERENA • CHILE / NOVEMBER 12 - 16, 2024

Proceedings of the 17th Pan-American Conference on Soil Mechanics and Geotechnical Engineering (XVII PCSMGE), and 2nd Latin-American Regional Conference of the International Association for Engineering Geology and the Environment (IAEG), La Serena Chile, 2024.

Insights into the characterization of subsurface geological faults from geomechanical models

Percepções sobre a caracterização de falhas geológicas em subsuperfície a partir de modelos geomecânicos

Roberto Quevedo
Tecgraf Institute, PUC-Rio, Brazil, rquevedo@tecgraf.puc-rio.br

Karoline Nunes, Francisco Corrêa Dias, Deane Roehl
Department of Civil and Environmental Engineering and Tecgraf Institute, PUC-Rio, Brazil

Bruno R. B. M. Carvalho
Petrobras Research Center, Petrobras, Brazil

ABSTRACT: Geological faults impact significantly several engineering fields since they may trigger earthquakes, well failures, surface settlement and flow path changes within aquifers and oil reservoirs. In order to understand such phenomena, extensive efforts have been made with a focus on the characterization of fault zones through outcrop observations and seismic data. Alternatively, numerical methods have been proposed for modeling geologic problems, particularly those associated with geomechanical issues. In this study, we employ the finite element method to model fault damage zones' formation processes. Two constitutive models capable of representing different deformation mechanisms are adopted to evaluate plastic regions, identifying them as damage zones. Conceptual models featuring a single fault are analyzed and compared in terms of the triggered plastic regions and the stress paths at representative points around the fault. The results show that the proposed methodology is well suited to reproduce the different deformation mechanisms along the fault and can help explain the fundamental questions regarding how fault damage zones in different rocks form and evolve.

KEYWORDS: Geological faults, fault damage zones, finite element analysis, geomechanics.

1 INTRODUCTION

In geology, a fault is usually considered any surface where rock shear displacements are observable. Such a definition is almost identical to that of a shear fracture, sometimes called micro-faults (Fossen, 2016). However, most geologists recognize that faults also include a volume of complexly deformed rock in a region called fault zone (Caine et al., 1996), which presents a definable width. Such a zone is composed by two structural domains, commonly named fault core with the main slip surface and the surrounding volume known as the fault damage zone. In general, the width of the fault core is in the order of millimeters to meters. On the other hand, the damage zone is characterized by a density of structures, including deformation bands and shear and tensile fractures. That zone can significantly impact hydrocarbon production, presenting much higher or significantly lower permeabilities than the protolith (Caine et al., 1996; Choi et al., 2016; Hennings et al., 2012; Paul et al., 2007).

Therefore, significant efforts have been made to characterize fault damage zones, in particular, considering outcrop observations. In those studies, statistical relationships are used to measure damage zone widths considering fault attributes such as fault displacement. However, weathering processes and conditions different from those in the subsurface do not allow a proper understanding of the deformation mechanisms that occurred along the fault (Quevedo et al., 2023). In addition, geophysical techniques have been proposed to characterize deep faults usually found in oil and gas fields. Unfortunately, most conventional seismic data rarely allow the characterization of fault damage zones due to interpretation uncertainties.

Alternatively, numerical modeling emerged as an alternative to understanding the formation and evolution of damage zones through techniques such as the discrete element method (DEM) or the finite element method (FEM). Although the former has been used in several applications (Botter et al., 2014, 2016; Schöpfer et al., 2007), FEM has been recognized due to its flexibility for modeling geologic problems, particularly those associated with geomechanical issues (Gray et al., 2014).

In recent years, some studies have been published based on the results of GEOBAND, a Brazilian research and collaboration project for understanding and modeling fault damage zones in carbonate rocks. Those studies consider FEM and elastoplastic constitutive models for modeling damage zones. (Lima et al., 2020, 2021; Lima, 2021) proposed a methodology for modeling shear bands in plug scale. Andrade et al. (2020), Andrade (2021), and Quevedo et al. (2023) proposed a methodology based on the application of suitable boundary conditions in conceptual models to assess the width of damage zones in single faults. Nunes et al. (2022) and Nunes (2023) presented a procedure for modeling linking damage zones between geologic faults. Congro et al. (2023) proposed regression models to obtain damage zone widths considering the impact of geomechanical properties in sandstone reservoirs. Those studies demonstrate that geomechanical models with FEM, elastoplastic models, and more elaborate loading conditions can be well suited to reproduce the different deformation mechanisms around geological faults.

Based on the results of the mentioned studies, we provide some insights into the characterization of subsurface geological faults in this paper. First of all, a summary of the proposed methodology based on FEM and suitable boundary conditions is presented. Two elastoplastic models, the Soft Rock Plasticity (SR3) and the Mohr-Coulomb (MHC), are used to represent the geomechanical behavior of host rocks. Then, some conceptual models considering a single fault are presented and analyzed in terms of the resultant deformation mechanisms and stress paths at representative observation points around the fault. Finally, a parametric study is performed to check the impact of geomechanical parameters on the definition of fault damage zones.

2 METHODOLOGY

The methodology presented in this study has been documented in previous studies published in the literature: Andrade (2021), Quevedo et al. (2023), and Congro et al. (2023). In the first step, a normal fault, such as surface F1, is intersected with a vertical plane, as shown in Figure 1a. Over F1, we assume a contour of displacements with the highest values (black regions on the fault) concentrated in the central region and null values (white regions on the fault) around the tips. The transition between the displacements of those regions follows a parabolic distribution.

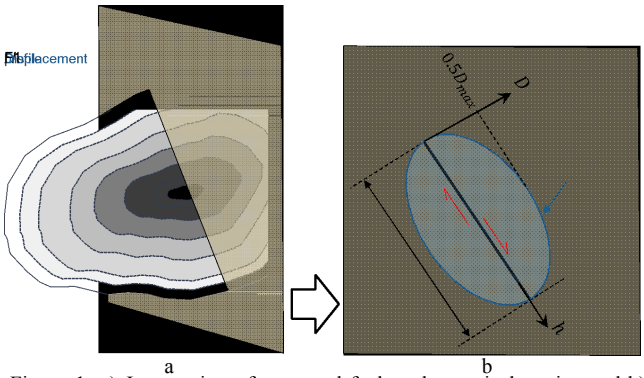

Figure 1. a) Intersection of a normal fault and a vertical section and b) representation of the 2D model with the line representing the fault discontinuity and the corresponding displacement profile.

In the second step, the intersection line and the corresponding displacement contour are extracted in the vertical section, as shown in Figure 1b. In that figure, the fault is represented by its height (H) and the maximum relative displacement (D_{max}). Field data based on outcrop observations have shown that D_{max} can vary between 1% and 20% of H (Kim & Sanderson, 2005; Kolyukhin & Torabi, 2012; Schultz et al., 2008). Therefore, in this study, we assume that D_{max} is proportional to 10% of H and evenly distributed on both sides of the fault. Field observations show that in an idealized model of a single fault, the displacement profile may vary from linear to bell-shaped or elliptic, with the highest values near the fault surface center and null values at the fault tips (Quevedo et al., 2023).

Moreover, the relative displacement profile (D) follows a parabolic distribution given as

$$D = -4D_{max}\left(\frac{h}{H}\right)^2 + 4D_{max}\left(\frac{h}{H}\right) \quad (1)$$

where h is the distance measured from the tip at the top of the fault.

In the third step, the fault line is duplicated, but the tips are the same. Over each superposed line, the cumulative displacement profile is applied incrementally according to the direction of the red arrows indicated in Figure 1b. Observe that those movements are imposed to represent a normal fault in which the hanging wall moves down relative to the footwall. Then, due to the imposed displacements, plastic deformations are triggered in the host rock near the fault line. The geomechanical behavior of the rock is represented through the SR3 model (Crook et al., 2006) given by the following yielding function:

$$F_{SR3} = g_\sigma q - (p - p_t)tan\beta\left(\frac{p-p_c}{p_t-p_c}\right)^{\frac{1}{n_y}} \quad (2)$$

where p is the mean effective stress, q is the deviatoric stress, and g_σ is a function that defines the shape of the plasticity surface in the deviatoric plane according to variations of Lode angle. For further details about this function, see Nunes (2023).

The parameters β, p_t, p_c, and n_y define the shape of the plasticity surface in the $p - q$ plane. The parameters p_c and p_t define the yield stresses in hydrostatic compression and tension, respectively. Both can vary with the occurrence of plastic deformations. However, due to the lack of experimental data to represent such variation, both parameters were considered fixed in this study. Therefore, neither hardening nor softening are adopted in the present simulations. For comparison purposes, the Mohr-Coulomb model (MHC) is also used to represent the geomechanical behavior of the host rock. The following yielding function represents the MHC model:

$$F_{MHC} = g_\sigma q - (p - p_t)tan\beta \quad (3)$$

In order to make fair comparisons between the SR3 and the MHC models, g_σ=1 was adopted in both models, getting rid of the Lode angle dependence. Figure 2 compares the yielding surfaces of SR3 and MHC and the different plastic deformation mechanisms. As can be seen, the MHC can simulate pure and shear dilation mechanisms. However, the SR3 is capable of simulating those mechanisms and shear and pure compaction.

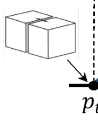

Figure 2. Comparison between yield surfaces of MHC and SR3 including regions with different plastic deformation mechanisms.

To complete the formulation of the models, plastic potential functions similar to those of their corresponding yield functions are adopted. However, a non-associative flow rule is adopted by considering the dilatancy angle (Ψ) instead of β. Moreover, linear elastic behavior is adopted considering the Young's modulus (E) and the Poisson's ratio ( ). The damage zone is assumed to be the region with plastic deformations, quantified through the variable *PEMAG* defined as

$$PEMAG = \sqrt{\frac{2}{3}\left(\varepsilon_{P1}^2 + \varepsilon_{P2}^2 + \varepsilon_{P3}^2\right)} \quad (4)$$

where ε_p is the principal plastic strain vector. In order to define the boundaries of the damage zone, a minimum threshold value of $PEMAG$ ($PEMAG_{min}$) was defined as 0.1.

3 ANALYSIS OF CONCEPTUAL MODELS

In this study, we adopt conceptual models of a single fault with a height of 500 m and a dip of 60°. In order to represent conditions similar to those of a Brazilian pre-salt field, the fault center is located at 5000 m depth. The model's top and bottom depths are 4250 and 5750 m, respectively. For such depths, the vertical and horizontal effective stresses at the top are 27 MPa and 24 MPa, respectively. The stresses at the bottom are computed by adopting an effective stress gradient of 0.012 MPa/m.

The mesh is composed by 6712 nodes and 2209 quadrilateral elements of quadratic interpolation and full integration (CPE8), as shown in Figure 3. The model boundaries are far from the line fault to avoid influencing the results. A refined discretization is employed around the fault region to better resolve the stress concentration.

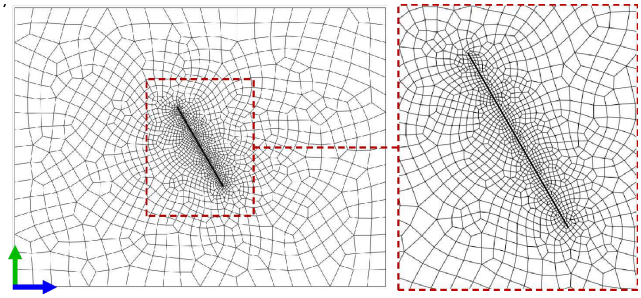

Figure 3. Finite element mesh adopted for the modeling of damage zones in a single fault.

The following properties were adopted to represent the geomechanical behavior of the host rock.

Table 1. Material properties used to represent the host rock.

Parameter	*Value*
Young modulus, E (GPa)	17.0
$Poisson\ ratio$, (-)	0.3
Friction angle, β (degree)	54.0
Dilatancy angle, Ψ (degree)	43.3
Yield stress in hydrostatic expansion, p_t (MPa)	8.9
Shape parameter, n_y (-)	2.5

In total, three models are analyzed in this study, one considering the MHC model and the other two with the SR3 model adopting p_c values of 240 and 70 MPa. Those values are representative of well and poorly consolidated carbonate rocks (Fisher et al., 2018) and are adopted to check the impact of the p_c parameter in the development of damage zones. The analyses are performed with the software Abaqus® using the solver for large displacements.

Figure 4 shows a comparison between the resultant $PEMAG$ distribution around the fault considering the three models. In the MHC model, high-intensity plastic deformations ($PEMAG > 1.0$) are concentrated in a narrow region around the fault line. In turn, in the SR3 models, such regions are more distributed along the fault. Another significant difference among the results is the shape of the plastic deformation contours at the fault tips. While the MHC model clearly concentrates plastic deformation at tips, such concentrations are significantly reduced in the SR3 models, particularly in the model with p_c equal to 240 MPa. Another difference is the shape of the plastic regions. In the MHC model, the triggered damage zone seems to be anti-symmetric, with higher plastic deformations in the compression regions in the hanging wall and footwall. Such shape is also seen in the SR3 model with the higher p_c, but it is less noticeable. On the other hand, the model with the lower p_c shows an almost symmetrical shape.

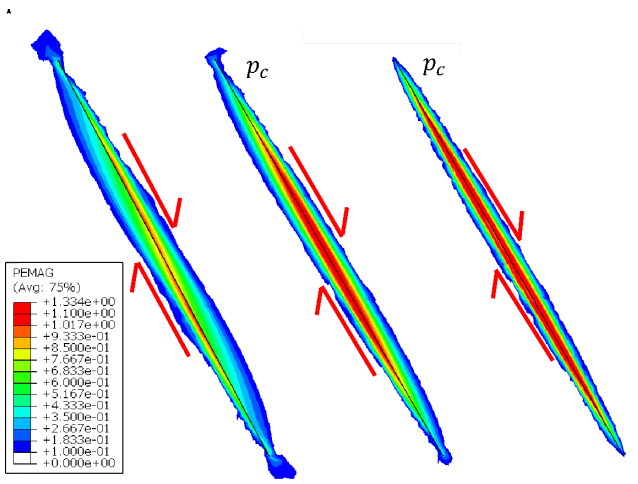

Figure 4. Plastic regions around the fault considering the MHC and the SR3 models.

Figure 5 shows the stress paths obtained at three observation Gauss points over the hanging wall, around the fault line, and within the damage zone. Those points are: A at the upper tip, B in the central region, and C at the lower tip. The stress paths correspond to the results obtained with the MHC and SR3 models with p_c = 240 MPa.

The stress paths at point A start from the same mean stress (p= 28 MPa) and then go to the left, showing tensile and deviatoric stress increments within the elastic domain. Once the stress paths reach the yield envelopes at $p \approx 20$ MPa, they go to the right with shear-dilation plastic deformations (see Figure 2), reaching a mean stress of approximately 29 MPa. Then, the stress paths change direction and go to the left until getting close to the yield stress in hydrostatic expansion $p = p_t$. This non-monotonic behavior observed in the MHC and SR3 models can be explained by the occurrence of compressive plastic strain increments immediately after yielding. Such increments appear as a result of the compression triggered by regions around the upper tip of the fault. However, after a certain deformation level, dilatant plastic strain increments occur as a consequence of the mechanical dilation of the surrounding rock.

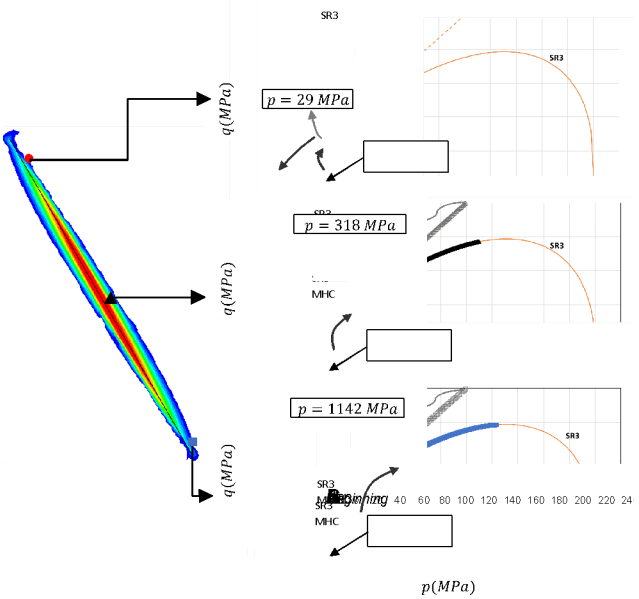

Figure 5. Stress paths obtained with the MHC and SR3 (p_c=240 MPa) corresponding to three observation points. Adapted from Nunes (2023).

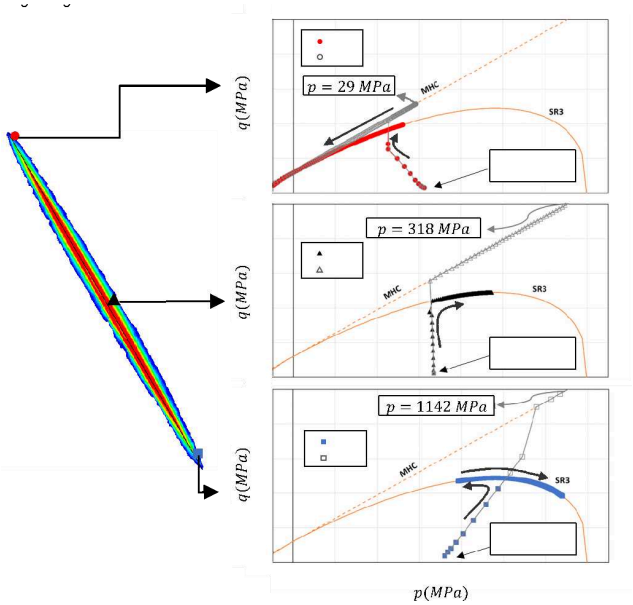

Figure 6. Stress paths obtained with the MHC and SR3 (p_c=70 MPa) corresponding to three observation points. Adapted from Nunes (2023).

The stress paths at point B present pure deviatoric stresses within the elastic domain. Once the stress paths reach the yield envelopes, they go to the right with shear-dilation plastic deformations, significantly increasing their mean stresses, reaching 150 MPa and 318 MPa in the SR3 and MHC models, respectively.

The stress paths at point C show elastic compressive stresses in the elastic domain. Once the stress paths reach the envelopes, they go to the right similarly to that observed at point B. However, in this case, the mean stress reached by the SR3 model (163 MPa) is significantly lower than that obtained with the MHC model (1142 MPa).

The differences observed in the final mean stresses at points B and C can be explained by the difference between the shapes of the plastic potential functions of the MHC and the SR3 models. During the simulations, the MHC model continuously triggers plastic shear-dilation with the same rate during the evolution of the stress path. In practical terms, such dilation rate is much larger than that observed in soils and rocks. On the other hand, the dilation rate is reduced in the SR3 model as the stress path enters the transition zone (see Fig. 2). Thus, the total dilatant plastic strain is lower in the SR3 model than in the MHC model. Consequently, the final mean stress in the SR3 model, at points B and C, results significantly lower than that obtained with the MHC model. The capability of the SR3 model to hold dilatant plastic strains is an advantage of elastoplastic models with CAP.

Figure 6 shows the stress paths corresponding to the results obtained with the MHC and the SR3 models with p_c=70 MPa at the observation points in Figure 5. In this case, the size of the yield surface is much lower than in the previous case due to the reduced yield stress in hydrostatic compression. The stress paths at point A are very similar to those observed in Figure 5, showing a non-monotonic behavior. This result shows that the stress path at point A is practically unaffected by the size of the yield envelope of the SR3 model.

Once again, the stress paths at point B present pure shear stress within the elastic domain. Once they reach their corresponding yield envelopes, they go to the right. However, different from the previous case that reached p = 150 MPa, the mean stress in the SR3 model now reaches a maximum value of 47 MPa.

The stress path with the SR3 model at point C shows compressive stress increments in the elastic domain, similar to the stress path observed with a lower p_c. However, when the stress path reaches the yield envelope in the transition zone, it goes to the left, showing reductions in the mean stress until reaching a value of 38 MPa. Then, the stress path changes direction and goes to the right with significant increments in the mean stress, reaching values of 64 MPa. This non-monotonic behavior observed in the SR3 model can be explained by the occurrence of local plastic dilation in the lower tip of the fault during the application of the first displacements. However, after the application of a certain displacement level, the mean stress increases as a consequence of the mechanical compaction of the surrounding rock.

Further simulations were performed to evaluate the impact of the other geomechanical parameters (E, , β, and Ψ) on the assessment of the damage zone considering the SR3 model with an intermediate value for hydrostatic yield in compression (p_c = 120 MPa). In this group of simulations, one parameter at a time was changed while the others remained constant. In order to compare the results, the damage zone width (W) is measured through a path normal to the fault dip that crosses it by its center. The results confirmed that neither the elastic parameters nor the friction angle affect the development of the damage zone. Indeed, only the variation of the dilatancy angle (Ψ) seems to affect the damage zone width, but only from a certain level of displacement ($D > 10$ m), as shown in Figure 7. From that displacement, the evolution of W is different among the three models, with larger damage zone widths for lower dilatancy angles.

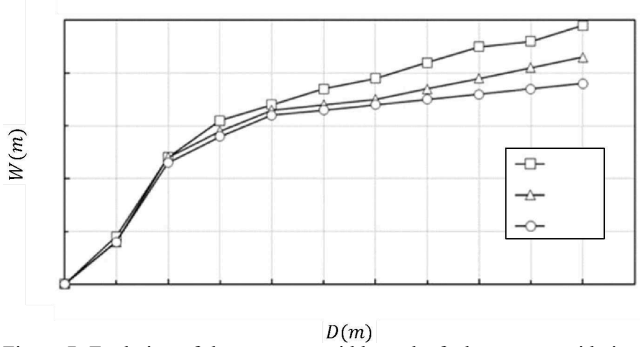

Figure 7. Evolution of damage zone widths at the fault center considering different dilatancy angles. Adapted from Nunes (2023).

Those results can be explained through Figure 8, which shows a diagram of volumetric plastic strains ($\Delta\varepsilon^{P}_{vol}$) vs deviatoric plastic strains ($\Delta\varepsilon^{P}_{dev}$) with the plastic potential envelopes of the models with the lowest and the largest dilatancy angles. The lower Ψ value, the larger the influence of the deviatoric component in the plastic strain increment, resulting in higher plastic strains and, consequently, larger damage zone widths.

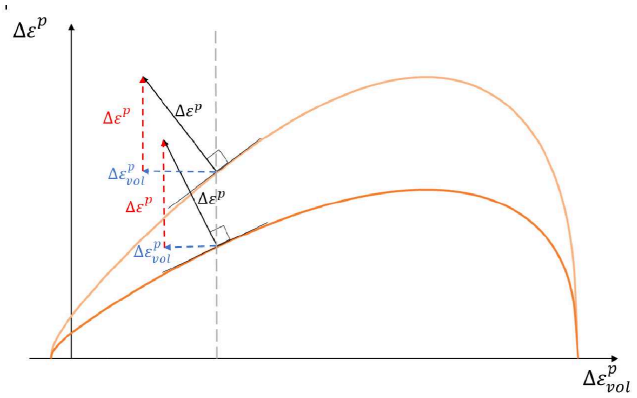

Figure 8. Evolution of damage zone widths at the fault center considering different dilatancy angles. Adapted from Nunes (2023).

4 CONCLUSIONS

In this study, we present a methodology for numerical modeling of fault damage zones using FEM, elastoplastic models, and suitable boundary conditions for the application of fault displacements. Two constitutive models are adopted for the representation of the geomechanical behavior of carbonate rocks in conditions similar to those of Brazilian Pre-salt fields: the Mohr-Coulomb model (MHC) and the Soft Rock model (SR3) with two yield stresses in hydrostatic compression (p_c=240 MPa and p_c=70 MPa). The comparison of plastic regions assessed through the equivalent plastic deformation (*PEMAG*) shows that the MHC model triggers anti-symmetric damage zones between the hanging wall and the footwall. In contrast, the models with the SR3 model seem to trigger symmetric damage zones around the fault. From the comparison between the results of the MHC model and the SR3 with the higher p_c, we notice similar stress paths with shear-dilation at the three observation points located around the fault over the hanging wall. On the other hand, the SR3 model with the lower p_c presents a stress path different from that observed in the MHC model due to the occurrence of shear-compaction, which cannot be reproduced in the latter model. These results show that elastoplastic models with CAP, such as the SR3, are the best choice for modeling the geomechanical behavior of rocks, particularly those that present reduced yield stresses in hydrostatic compression. The results show that the proposed methodology can be adopted to assess different deformation mechanisms in the damage zone around the fault, such as shear-dilation observed at points A and B, and shear-compaction observed at point C, as depicted in figures 5 and 6. From the parametric analysis, it was observed that only the dilatancy angle affects the evolution of the damage zone widths. That is expected since such an angle defines the shape of the plastic potential envelope, which in turn defines the plastic strains related to the damage zones. Further studies are under development in order to consider hardening and softening processes in the constitutive models and to check how they can affect the rock properties as well as the development of damage zones.

5 ACKNOWLEDGEMENTS

This research was carried out in association with the ongoing R&D project registered as ANP n◦ 21475-9, “GeoBanD 2 – Geomodelagem de zona de dano em falhas geológicas” (PUC-Rio/CENPES/ANP), sponsored by Petrobras. The authors also gratefully acknowledge the support from Carlos Chagas Filho Foundation for Supporting Research in the State of Rio de Janeiro (FAPERJ) Grant E-26/211.766/2021-0, Brazilian National Council for Scientific and Technological Development (CNPq) Grants 141617/2020-9, 420074/2021, and 407388/2022-2, and Tecgraf/PUC-Rio Institute. This study was financed in part by the Coordenação de Aperfeiçoamento de Pessoal de Nível Superior - Brazil (CAPES) - Finance Code 001.

6 REFERENCES

Andrade, T. J. . D. (2021). *Computational modeling of the formation and evolution of damage zones in geological faults [In Portuguese]*. Pontifical Catholic University of Rio de Janeiro.

Andrade, T. J. . D., Quevedo, R., Carvalho, B. R. B. M., & Roehl, D. (2020). Computational modeling of formation and evolution of damage zones in reservoir scale. *Proceedings of the XLI Ibero-Latin-American Congress on Computational Methods in Engineering*, *December*, 1–7.

Botter, C., Cardozo, N., Hardy, S., Lecomte, I., & Escalona, A. (2014). From mechanical modeling to seismic imaging of faults: A synthetic workflow to study the impact of faults on seismic. *Marine and Petroleum Geology*, *57*, 187–207.

Botter, C., Cardozo, N., Hardy, S., Lecomte, I., Paton, G., & Escalona, A. (2016). Seismic characterisation of fault damage in 3D using mechanical and seismic modelling. *Marine and Petroleum Geology*, *77*, 973–990.

Caine, J. S., Evans, J. P., & Forster, C. B. (1996). Fault zone architecture and permeability structure. *Geology*, *24*(11), 1025–1028.

Choi, J. H., Edwards, P., Ko, K., & Kim, Y. S. (2016). Definition and classification of fault damage zones: A review and a new methodological approach. *Earth-Science Reviews*, *152*, 70–87.

Congro, M., Zanatta, A. S., Nunes, K., Quevedo, R., Carvalho, B. R. B. M., & Roehl, D. (2023). Determination of fault damage zones in sandstone rocks using numerical models and statistical analyses. *Geomechanics for Energy and the Environment*, *36*, 100495.

Crook, A. J. L., Willson, S. M., Yu, J. G., & Owen, D. R. J. (2006). Predictive modelling of structure evolution in sandbox experiments. *Journal of Structural Geology*, *28*(5), 729–744.

Fisher, Q., Grattoni, C., Yielding, G., Freeman, B., & Michie, E. (2018). *Impact of faults in carbonate reservoir. CARBFAULT - Phase I. Final Report.*

Fossen, H. (2016). *Structural Geology*. Cambridge University Press.

Gray, G. G., Morgan, J. K., & Sanz, P. F. (2014). Overview of continuum and particle dynamics methods for mechanical modeling of contractional geologic structures. *Journal of Structural Geology*, *59*, 19–36.

Hennings, P., Allwardt, P., Paul, P., Zahm, C., Reid, R., Alley, H., Kirschner, R., Lee, B., & Hough, E. (2012). Relationship between

fractures, fault zones, stress, and reservoir productivity in the Suban gas field, Sumatra, Indonesia. *AAPG Bulletin*, *96*(4), 753–772.

Kim, Y. S., & Sanderson, D. J. (2005). The relationship between displacement and length of faults: A review. *Earth-Science Reviews*, *68*(3–4), 317–334.

Kolyukhin, D., & Torabi, A. (2012). Statistical analysis of the relationships between faults attributes. *Journal of Geophysical Research: Solid Earth*, *117*(5).

Lima, R. S. B. De, Quevedo, R., Carvalho, B. R. B. M., & Roehl, D. (2021). Numerical modeling of shear bands in rocks using FEM and a viscous regularization technique. *Proceedings of the XLII Ibero-Latin American Congress on Computational Methods in Engineering Ibero-Latin American Congress on Computational Methods in Engineering*, *January 2022*, 1–7.

Lima, R. S. B. De, Quevedo, R., & Roehl, D. (2020). Computational modeling of deformation bands in a plug scale. *XLI CILAMCE – Ibero-Latin American Congress on Computational Methods in Engineering*, *December*.

Lima, R. S. B. (2021). *Computational Modeling of Shear Bands in Plug Scale [In Portuguese]*. Pontifical Catholic University of Rio de Janeiro.

Nunes, K. (2023). *Numerical modeling using the finite element method for characterization of fault damage zones [In Portuguese]*. Pontifical Catholic University of Rio de Janeiro.

Nunes, K, Quevedo, R., Roehl, D., & Carvalho, B. R. (2022). Numerical modeling of the linking damage zone between geologic faults. *Proceedings of the Joint XLIII Ibero-Latin-American Congress on Computational Methods in Engineering*, *7*.

Paul, P., Zoback, M., & Hennings, P. (2007). Fluid Flow in a Fractured Reservoir Using a Geomechanically-Constrained Fault Zone Damage Model for Reservoir Simulation. *Proceedings of SPE Annual Technical Conference and Exhibition*, 1–2.

Quevedo, R., de Andrade, T. J., Santos, L., Carvalho, B. R. B. M., & Roehl, D. (2023). Assessment of fault damage zones in carbonate rocks based on numerical and sensitivity analyses. *Tectonophysics*, *864*(August), 230023. https://doi.org/10.1016/j.tecto.2023.230023

Schöpfer, M. P. J., Childs, C., & Walsh, J. J. (2007). Two-dimensional distinct element modeling of the structure and growth of normal faults in multilayer sequences: 2. Impact of confining pressure and strength contrast on fault zone geometry and growth. *Journal of Geophysical Research: Solid Earth*, *112*(10), 1–16.

Schultz, R. A., Soliva, R., Fossen, H., Okubo, C. H., & Reeves, D. M. (2008). Dependence of displacement-length scaling relations for fractures and deformation bands on the volumetric changes across them. *Journal of Structural Geology*, *30*(11), 1405–1411.